PHYSICAL REVIEW C VOLUME 25, NUMBER 2 FEBRUARY 1982

Sub-barrier fusion of ^{58,64}Ni with ^{64}Ni and ^{74}Ge

M. Beckerman, M. Salomaa, A. Sperduto,* and J. D. Molitoris[†]
Laboratory for Nuclear Science, Massachusetts Institute of Technology, Cambridge, Massachusetts 02139

A. DiRienzo[‡]
Laboratory for Nuclear Science, Massachusetts Institute of Technology, Cambridge, Massachusetts, 02139
and Physics Department, United States Military Academy, West Point, New York 10996

(Received 27 July 1981)

Differential cross sections for evaporation residue formation following complete fusion of ^{64}Ni and ^{74}Ge with 171 to 215 MeV ^{58}Ni and ^{64}Ni ions were measured with high precision using a velocity selector together with a counter telescope. The resulting excitation functions for complete fusion ranged in magnitude from 10 μb to 300 mb. The excitation functions exhibited a strong response, at sub-barrier energies, to changes in the underlying nuclear structure. We interpreted these variations as evidence that the fusion proceeds through dynamic single-particle/softness-related processes. A phenomenological analysis was performed. In the analysis, we employed the Wentzel-Kramers-Brillouin method, constructed a simple interaction potential and introduced a radially-dependent effective mass. The use of the variable effective mass led to a meaningful description of our above-barrier data and to improvements towards describing our sub-barrier data.

NUCLEAR REACTIONS Complete fusion, ^{58}Ni + ^{64}Ni, ^{58}Ni + ^{74}Ge, ^{64}Ni + ^{58}Ni, ^{64}Ni + ^{64}Ni, ^{64}Ni + ^{74}Ge, $E = 171$ to 215 MeV (lab), measured σ (E,θ) for evaporation residues; observed dynamic, single-particle/softness effects; performed barrier-penetration analysis.

I. INTRODUCTION

The fusion of heavy ions is often described in terms of adiabatic passage through or over a one-dimensional fusion barrier. In these descriptions the fusion barrier represents that portion of the (real) interaction potential where the nuclear attraction becomes stronger than the Coulomb and centrifugal repulsion.[1] The dynamics of the fusion process is then characterized by the corresponding transmission coefficients. The characterization is equivalent to assuming ingoing wave boundary conditions,[2] or equivalently,[2] to assuming that the nucleus is "black"[3] so there are no reflections from the nuclear interior. Many observed features of heavy-ion fusion at above-barrier energies can be reproduced within this framework. In contrast, the process by which nuclei, particularly massive ones, fuse at sub-barrier energies is not understood. This process is of great interest as it may provide information on the interplay between fusion dynamics and the underlying nuclear structure, and it may serve as a probe of the nuclear potential as far into the nuclear interior as the inner turning point of the interaction potential.

The lack of insight into the sub-barrier fusion process is due, in large measure, to a paucity of experimental data. To remedy this situation a program was initiated of high precision measurements of excitation functions for complete fusion of massive nuclei at sub-barrier energies. A brief summary of the most salient features of the excitation functions for the ^{58}Ni + ^{58}Ni, ^{58}Ni + ^{64}Ni, and ^{64}Ni + ^{64}Ni systems has been presented in a recent Letter.[4] A detailed account of the experimental method and results for the ^{58}Ni + ^{58}Ni system has also been published.[5] In this work we present a thorough summary of our findings for the ^{58,64}Ni + ^{64}Ni and ^{58,64}Ni + ^{74}Ge systems. The three Ni-Ni systems involve closed-shell (vibrational) nuclei plus a number of valence neutrons. The extension of the measurements to the midshell (rotational) ^{74}Ge nucleus is a natural one; the present cycle of measurements will be closed upon completion of the Ge-Ge measurements now in progress.

In the experiments, 171 to 215 MeV ^{58}Ni and ^{64}Ni beams provided by the BNL tandem Van de Graaff facility were used to bombard isotopically enriched ^{58}Ni, ^{64}Ni, and ^{74}Ge targets. Differential cross sections for evaporation residue formation were measured using the MIT-BNL recoil mass selector (RMS) together with a ΔE-E telescope. The experimental setup and procedure are discussed in Sec. II. At the energies involved in the measurements fission competition is negligible, and the evaporation residue cross sections equal the complete fusion cross sections. The differential cross sections for evaporation residue formation and comparisons of the resulting sub-barrier fusion excitation functions are presented in Sec. III.

We then analyzed the excitation functions; our objective was to further our understanding of the structural/dynamic content of the data. We constructed a phenomenological interaction potential and treated the barrier penetration aspects using the well-known WKB relation[6] between the action integral and the transmission coefficient. These analyses are presented and discussed in Sec. IV, and the work is summarized in Sec. V.

II. EXPERIMENTAL METHOD

The experimental setup and procedure has been described in detail in Ref. 5 (hereafter referred to as I). In brief, two silicon surface barrier detectors were mounted in the scattering chamber at angles of 21.8° with respect to the beam axis. The elastic scattering yields in these detectors were used for normalization and beam monitoring. The MIT-BNL velocity selector, or recoil mass selector (RMS), consisted of an electric/magnetic deflector, a Wien (velocity or $E \times B$) filter, and fore and aft magnetic quadrupole doublets. This system was used to separate the evaporation residue (ER) recoils from beam-tail, elastic scattering, and other types of events. Only that portion of the beam tail, produced by slit scattering, having the ER velocity was transmitted by the RMS. These events were well separated from the ER events in the ΔE-E spectra as can be seen in Fig. 1. The telescope ΔE section consisted of a proportional chamber containing isobutane at 20 mm Hg. The telescope E section consisted of a 450 mm^2 silicon surface barrier detector mounted at the rear of the gas chamber. The two monitor signals, and the telescope ΔE and E-ΔE signals were processed by conventional electronics, and collected and stored on line in the BNL Sigma-7 computer system.

Two well-known requirements for measuring ER recoils directly with high precision at sub-barrier energies are the ability to perform the measurements at forward recoil angles and the ability to distinguish, if not eliminate, other reaction/background events from the ER events. In the experiments we measured ER yields over angular ranges from 0° to 6° (see Sec. III). Pileup events were minimized by restricting the beam-tail countrate to the 10 to 50 counts/s range. Events arising from reactions with carbon and oxygen contaminants and events arising from partial momentum transfer processes[7] were eliminated by the RMS. Evaporation residue contributions from heavier isotopes of the target element were limited by using enriched targets. We see from Table I that the targets contained on the order of 0.1% heavier isotopes. Special care was taken to avoid "satellite" beams. A 98% enriched ^{64}Ni source was used and, in general, single-stripping operation was preferred. Finally, measurements for the ^{58}Ni + ^{64}Ni system were repeated with target and projectile reversed to confirm that no target or projectile contaminants were present. Representative ΔE-E spectra are shown in Fig. 1. It is clear that the ER identification was unambiguous and, in fact, there was considerable redundancy in the telescope information.

Differential cross sections for evaporation residue formation were obtained from the evaporation residue yields $Y_{\mathrm{ER}} = N_{\mathrm{ER}}^{tel}/N_{el}^{\mathrm{mon}}$ by means of the relation

$$\frac{d\sigma^{\mathrm{ER}}}{d\Omega}\left[\theta_{\mathrm{ER}}\right] = Y_{\mathrm{ER}} f^{-1} \frac{d\sigma^{\mathrm{Ruth}}}{d\Omega}\left[\theta_{\mathrm{mon}}\right].$$

In this expression $d\sigma^{\mathrm{Ruth}}/d\Omega$ is the calculated differential cross section for Rutherford scattering at the target chamber monitor angle, and f^{-1} is the inverse absolute efficiency of the detection system. The absolute efficiencies were determined by elastically scattering ions of similar atomic and mass numbers, and kinetic energy, as the evaporation residues into the detection system. The calibration measurements discussed in I were extended to lower kinetic energies. The quantities f^{-1} were found to increase uniformly with decreasing reduced velocity over the entire energy range spanned in I and in the present work.

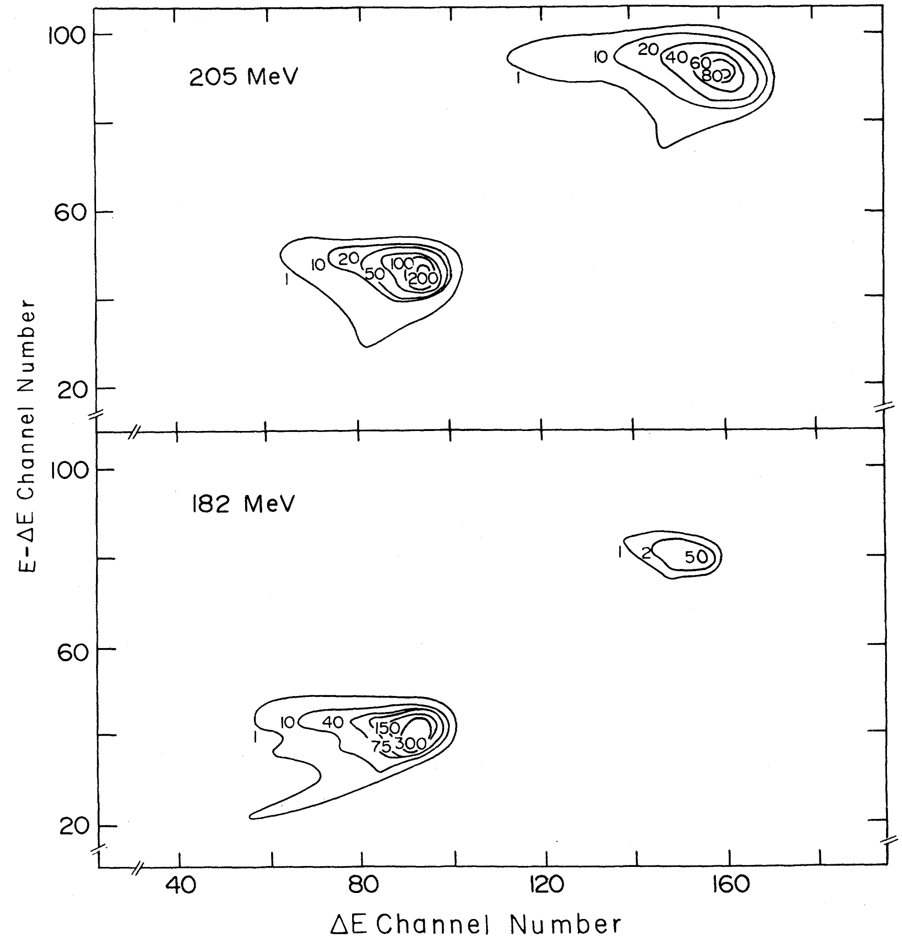

FIG. 1. Contour plots of E-ΔE vs ΔE obtained in the counter telescope at 0°. The projectile-target combination is ^{58}Ni + ^{74}Ge. The two concentrations of counts represent transmitted beam-tail (lower $\Delta E,E$) events and evaporation residue (higher $\Delta E,E$) events. These plots represent data taken with typical E resolution and worse than typical ΔE resolution. Collection times were less than 20 min for the 205 MeV data and about 45 min for the 182 MeV data.

TABLE I. Targets used in the measurements and their composition.

Target[a]	Thickness (μg/cm^2)	Purity (%)	Principal contaminants (%)
^{58}Ni	120	99.93	<0.1 other Ni isotopes
^{64}Ni	70 to 125	96.45	1.89 ^{58}Ni
			1.10 ^{60}Ni
			0.45 ^{62}Ni
			<0.2 Cr,Fe,Cu
^{74}Ge	90 to 200	98.90	0.26 ^{70}Ge
			0.49 ^{72}Ge
			0.20 ^{73}Ge
			0.15 ^{74}Ge

[a] On 6 to 20 μg/cm^2 formvar or carbon backings.

III. EXPERIMENTAL RESULTS

A. Differential cross sections

The measurements of differential cross sections for ER formation for the ^{58}Ni + ^{64}Ni, ^{64}Ni + ^{64}Ni, ^{58}Ni + ^{74}Ge, and ^{64}Ni + ^{74}Ge systems are summarized in Table II and Figs. 2 to 5. Table II lists the zero-degree differential cross sections integrated over the recoil kinetic energy spectra of the evaporation residues. As in I, all spectral integrations were performed using energy-dependent efficiencies and velocity acceptances, determined as part of the calibration. Errors presented in Table II are statistical errors; errors associated with the spectral integrations are on the order of 2%.

Recoil kinetic energy spectra, taken at representative bombarding energies and recoil angles, are displayed in Figs. 2 and 3. There are two features of note in these spectra. First, there is a substantial broadening of the ^{64}Ni + ^{64}Ni$\rightarrow$^{128}Ba* ER spectra (Fig. 2) as the recoil angle increases. This broadening is absent from the ^{58}Ni + ^{58}Ni$\rightarrow$^{116}Ba* ER spectra presented in I, and negligible to small in the ^{58,64}Ni + ^{74}Ge$\rightarrow$^{132,138}Nd* ER spectra (Fig. 3) and ^{58}Ni + ^{64}Ni$\rightarrow$ ^{122}Ba* ER spectra (not shown). Second, there is a narrowing of the ER spectra, at a given recoil angle, as the systems become more neutron rich. Both features are consequences of the systematic variations in the evaporation process for these proton-rich systems. Specifically, compound nuclei formed near the proton drip line such as ^{58}Ni + ^{58}Ni$\rightarrow$^{116}Ba* predominately proton emit. Neutron emission increases relative to proton emission as the compound nuclei approach the region of stability, and alpha particle emission becomes distinctive for compound nuclei which are sufficiently neutron rich such as ^{64}Ni + ^{64}Ni$\rightarrow$^{128}Ba*.

The variations in the angular distribution shape are more pronounced than the variations in spectral width. Angular distributions of the ER's are shown in Figs. 4 and 5. These angular distributions were obtained by measuring differential cross sections over recoil angles from 0° to 6° in either $\frac{1}{2}$° or 1° steps. The beam axis was determined by "left-right" measurements for each angular distribution; corrections to the nominal beam-axis direction were $\sim$0.1°. Owing to the sharp decrease in yield with increase in recoil angle, the angular distributions were constructed using weighted laboratory angles. The differential cross sections displayed in the figures have been integrated over the kinetic energy spectra. In Figs. 4 and 5, the angular distributions which are more sharply peaked in the forward direction correspond to compound nuclei which have a greater tendency to emit neutrons. In addition, there is a distinct "dip" or "shoulder" in the angular distributions of the ER's from ^{64}Ni + ^{64}Ni$\rightarrow$^{128}Ba* in the vicinity of 3° signifying the presence of alpha emission.

B. Excitation functions

The cross sections for evaporation residue formation are listed in Table III. These cross sections were obtained from integration of the angular distributions and from the zero degree cross section results of Table II. The conversions of the zero degree differential cross sections to cross sections for evaporation residue formation were done making use of the smoothly-varying results of the angular distribution integrations. Errors given in Table III are total errors. The statistical errors are, in most instances, considerably less than the total errors. The main contributions to the total errors are from uncertainties in the absolute efficiencies due to minor variations in beam tuning, and from uncertainties in the mean charge-state identification.

The cross sections for evaporation residue formation for the four systems investigated in the work are displayed in Fig. 6 together with the corresponding cross sections for the ^{58}Ni + ^{58}Ni system investigated in I. We have also presented in Tables II and III, and in Fig. 6 cross sections for the target-projectile-reversed ^{64}Ni + ^{58}Ni system. Again, the ^{64}Ni + ^{58}Ni measurements were performed as a special check that there were no contributions either from other isotopes of the target and projectile or from satellite beams of the same isotope. The complete agreement between cross sections for ^{58}Ni + ^{64}Ni and those for ^{64}Ni + ^{58}Ni confirmed that no such contributions were present.

The excitation functions displayed in Fig. 6 span broad dynamic ranges, varying from about 10 μb at far sub-barrier energies to about 200 mb at above-barrier energies. *Shapes:* As pointed out previously[4] the Ni-Ni excitation functions vary in shape at sub-barrier energies. Direct comparisons of the shapes of the Ni-Ge excitation functions to the shapes of the Ni-Ni excitation functions can be misleading. To enable meaningful comparision, we formed reduced excitation functions. That is, we scaled the center-of-mass energies by fitted barrier

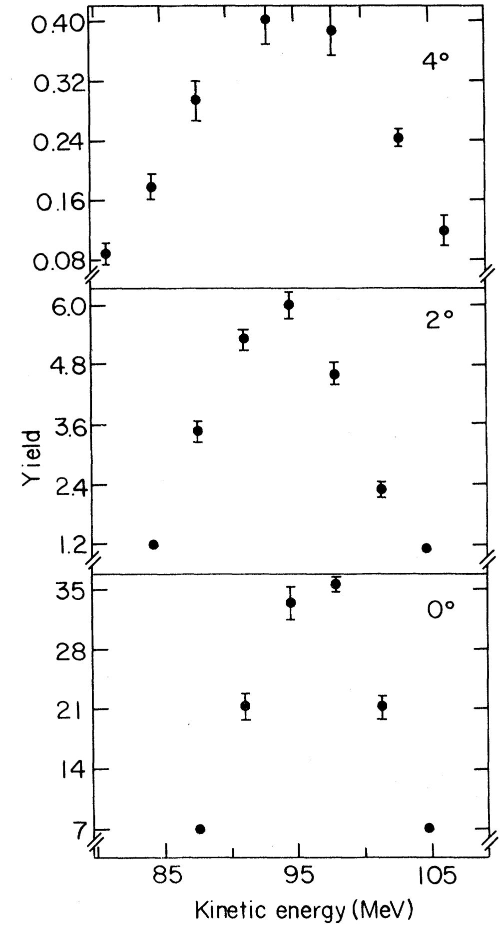

FIG. 2. Recoil kinetic energy spectra of the ^{64}Ni + ^{64}Ni $\rightarrow$ ^{128}Ba* evaporation residues. The spectra were taken at a bombarding energy of 205 MeV, at the indicated recoil angles.

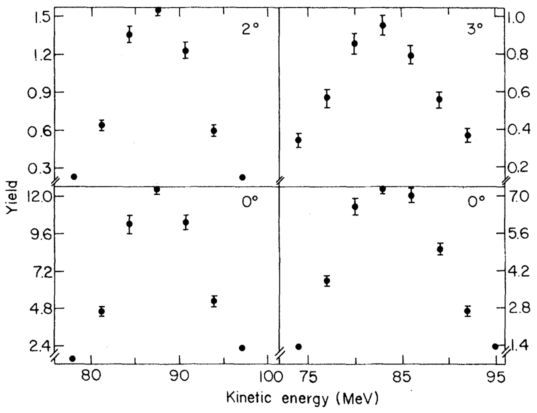

FIG. 3. Recoil kinetic energy spectra of the ^{64}Ni + ^{74}Ge $\rightarrow$ ^{138}Nd* evaporation residues (left-side pair) and ^{58}Ni + ^{74}Ge$\rightarrow$ ^{132}Nd* evaporation residues (right-side pair). These spectra were taken at 205 MeV, at the indicated recoil angles.

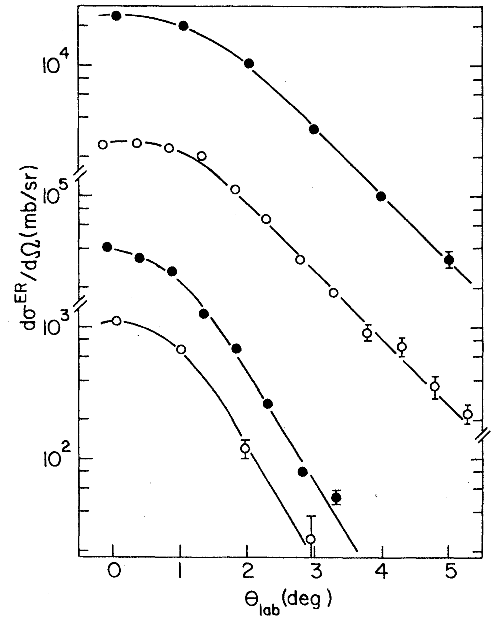

FIG. 4. Angular distributions of ^{58}Ni + ^{74}Ge $\rightarrow$ ^{132}Nd* evaporation residues (upper pair) and ^{64}Ni + ^{74}Ge$\rightarrow$ ^{138}Nd* evaporation residues (lower pair). Filled circles denote results at 205 MeV; open circles denote results at 190 MeV. Solid lines represent smoothed angular distributions used for integration purposes.

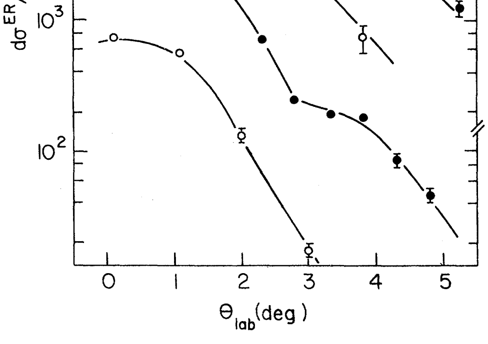

FIG. 5. Same as Fig. 4 for ^{58}Ni + ^{64}Ni$\rightarrow$ ^{122}Ba* evaporation residues (upper pair) and ^{64}Ni + ^{64}Ni $\rightarrow$ ^{128}Ba* evaporation residues (lower pair).

TABLE II. Summary of zero degree differential cross sections.

System	$E_{\text{c.m.}}$ (MeV)	$\frac{d\sigma^{\text{ER}}(0)}{d\Omega}$ (b/sr)	System	$E_{\text{c.m.}}$ (MeV)	$\frac{d\sigma^{\text{ER}}(0)}{d\Omega}$ (b/sr)
^{58}Ni + ^{64}Ni	109.5	57.86±3.02		94.5	11.25±0.63
	106.9	41.09±2.31		93.5	7.40±0.42
	104.3	34.37±2.25		92.5	3.84±0.34
	101.7	17.75±2.13		92.0	2.99±0.19
	99.3	13.36±0.73		91.5	2.29±0.30
	98.0	8.57±0.59		91.0	1.29±0.10
	97.2	8.83±0.61		90.6	0.723±0.095
	96.2	6.46±0.39		90.1	0.287±0.035
	95.9	5.13±0.25		89.6	0.103±0.025
	95.6	4.73±0.37	^{58}Ni + ^{74}Ge	120.0	37.78±1.79
	95.4	4.18±0.22		117.2	27.84±1.17
	95.1	4.34±0.30		114.1	23.42±0.76
	95.0	3.62±0.21		111.6	13.51±0.41
	94.9	3.45±0.15		108.8	7.20±0.29
	94.6	3.08±0.26		106.4	3.45±0.18
	94.4	2.64±0.15		106.0	2.42±0.16
	94.1	2.25±0.17		104.3	1.45±0.07
	93.9	2.13±0.19		102.7	0.430±0.035
	93.4	1.76±0.12		101.6	0.189±0.011
	92.8	1.20±0.10		100.4	0.0942±0.0100
	92.3	0.794±0.108		99.9	0.0464±0.0053
	91.8	0.500±0.069		99.6	0.0409±0.0065
	91.3	0.388±0.065		99.4	0.0282±0.0037
	90.8	0.204±0.033		98.8	0.0098±0.0025
	90.3	0.108±0.017	^{64}Ni + ^{74}Ge	114.8	79.94±3.19
	89.8	0.0284±0.0079		112.1	55.79±2.04
	89.3	0.0223±0.0037		109.4	40.56±2.20
^{64}Ni + ^{58}Ni	101.7	23.26±0.89		106.8	22.02±0.46
	99.3	15.61±0.66		104.1	8.12±0.17
	96.9	7.35±0.35		102.5	3.44±0.19
	94.6	2.73±0.12		101.2	1.13±0.06
	92.2	0.647±0.046		100.4	0.566±0.023
^{64}Ni + ^{64}Ni	106.9	92.15±3.93		99.3	0.212±0.016
	104.4	84.12±3.48		98.8	0.0829±0.0075
	101.9	59.77±1.97		98.3	0.0493±0.0049
	99.4	44.74±2.17		97.7	0.0108±0.0016
	96.9	26.28±0.86		97.5	0.0080±0.0016

heights and the cross sections by the squares of the corresponding fitted barrier positions for each excitation function. The scale variables are, *ipso facto,* model dependent. Therefore, we have displayed in Figs. 7 and 8 reduced excitation functions for two sets of scale variables. The phenomenological models used to fit the excitation functions for the five systems are discussed in Sec. IV. Although there are systematic differences between the two sets of scale variables, it can be seen that the relative behavior of the reduced excitation functions are not affected to any appreciable extent.

At above-barrier energies, the reduced excitation functions displayed in Figs. 7 and 8 approach one another. At far sub-barrier energies the reduced excitation functions differ from one another by up to two orders of magnitude. These differences are not accounted for by variations in barrier height and position, but instead arise from the interplay between fusion dynamics and the underlying nuclear structure. Specifically, we see that the penetrabilities for the Ni-Ge systems are greater

TABLE III. Summary of evaporation residue cross sections.

System	$E_{\mathrm{c.m.}}$ (MeV)	σ^{ER} (mb)	$\Delta\sigma^{\mathrm{ER}}$ (%)	System	$E_{\mathrm{c.m.}}$ (MeV)	σ^{ER} (mb)	$\Delta\sigma^{\mathrm{ER}}$ (%)
^{58}Ni + ^{64}Ni	109.5	308	15		94.5	30.5	12
	106.9	208	15		93.5	19.9	10
	104.3	166	15		92.5	10.1	15
	101.7	80.6	20		92.0	7.84	12
	99.3	59.7	9		91.5	6.01	20
	98.0	35.7	15		91.0	3.37	15
	97.2	35.7	12		90.6	1.88	18
	96.2	25.5	10		90.1	0.743	15
	95.9	20.1	10		89.6	0.265	25
	95.6	18.4	12	^{58}Ni + ^{74}Ge	120.0	203	12
	95.4	16.2	10		117.2	140	12
	95.1	16.6	12		114.1	110	10
	95.0	13.8	10		111.6	60.2	12
	94.9	13.1	10		108.8	30.4	12
	94.6	11.6	12		106.4	14.2	12
	94.4	9.90	10		106.0	10.6	10
	94.1	8.54	9		104.3	5.83	12
	93.9	7.93	15		102.7	1.69	15
	93.4	6.52	15		101.6	0.737	15
	92.8	4.41	15		100.4	0.362	15
	92.3	2.89	20		99.9	0.177	15
	91.8	1.80	20		99.6	0.156	20
	91.3	1.39	20		99.4	0.107	20
	90.8	0.722	20		98.8	0.0371	30
	90.3	0.377	20	^{64}Ni + ^{74}Ge	114.8	176	12
	89.8	0.098	30		112.1	115	12
	89.3	0.077	20		109.4	73.3	10
^{64}Ni + ^{58}Ni	101.7	100	10		106.8	40.5	12
	99.3	63.8	10		104.1	14.4	12
	96.9	28.8	9		102.5	5.94	12
	94.6	10.2	10		101.2	2.04	10
	92.2	2.33	11		100.4	0.966	12
^{64}Ni + ^{64}Ni	106.9	306	12		99.3	0.359	15
	104.4	267	12		98.8	0.140	15
	101.9	176	10		98.3	0.0831	15
	99.4	128	12		97.7	0.0182	20
	96.9	71.9	12		97.5	0.0133	25

than those for the Ni-Ni systems. The large increases in sub-barrier fusion for ^{58}Ni + ^{74}Ge are reduced somewhat for ^{64}Ni + ^{74}Ge, paralleling the ^{58}Ni + ^{64}Ni and ^{64}Ni + ^{64}Ni variations, while the increased sub-barrier fusion for ^{58}Ni + ^{64}Ni, relative to ^{58}Ni + ^{58}Ni, already apparent in Fig. 6 is clearly evident.

Magnitudes: The second major aspect of the fusion data concerns their magnitudes at far sub-barrier energies. In Refs. 4 and 5, the Ni-Ni excitation functions were compared to predictions of the generalized liquid-drop model of Krappe, Nix, and Sierk (KNS).[8] The potential in this model was similar to the proximity potential,[9] and doubly folding a Yukawa function over a sharp surface density distribution took into account both a finite range and a surface diffuseness. The result of comparisons[4] to the Ni-Ni data was that the observed cross sections were more than three orders of magnitude larger than the predicted cross sections at far sub-barrier energies. The differences in magnitude between observed and predicted cross sections reflect shifts in energy toward lower values. For the lowest measured cross sections (10

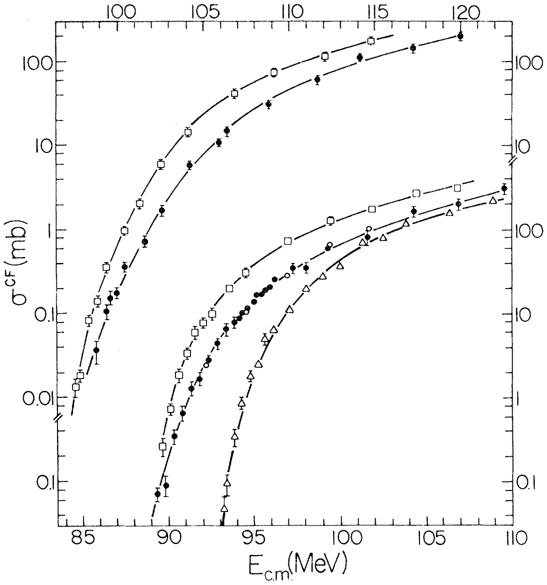

FIG. 6. Excitation functions for complete fusion. Constructed using weighted, average center-of-mass energies. Lower portion: ^{58}Ni + ^{58}Ni (open triangles), ^{58}Ni + ^{64}Ni (filled circles), ^{64}Ni + ^{58}Ni (open circles), and ^{64}Ni + ^{64}Ni (open squares). Upper portion: ^{58}Ni + ^{74}Ge (filled circles) and ^{64}Ni + ^{74}Ge (open squares). Smooth curves drawn through the data points are visual guides.

to 50 μb), the energy differences ranged from 5 to 7 MeV for Ni-Ni to more than 8 MeV for Ni-Ge.

A possible explanation, within a liquid-drop framework, for the large sub-barrier cross sections was that they were a consequence of zero-point motion. In a liquid-drop approach, large increases in penetrability may be possible for systems which, sufficiently massive, have fission barriers substantially lower than their fusion barriers. For our systems the fusion-fission barrier differences exceed 10 MeV. Calculations, which took into account average dynamic deformations as well as zero-point motion, have been done for the ^{58}Ni + ^{58}Ni system by Landowne and Nix.[10] In these calculations the interaction energy included monopole and quadrupole Coulomb terms, a nuclear term, a parabolic deformation energy, and centrifugal energy. The nuclear potential was the KNS form with constants from KNS and Möller-Nix.[11] The stiffness and inertia constants were derived from values given by Wong.[12] These, in turn, were determined from experimental $B(E2, 0^+ \rightarrow 2^+)$ values and energies of the first 2^+ state. As in the KNS calculation, no parameter adjustments were attempted. The result of the full (average dynamic deformation plus zero-point motion) calculation was an excitation function similar to that for penetration of a one-dimensional barrier by spherical nuclei.

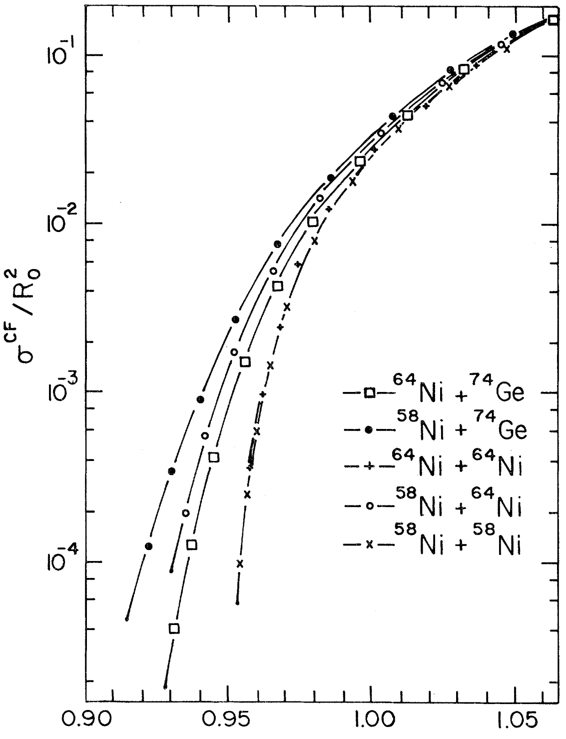

FIG. 7. Reduced excitation functions, plots of experimental excitation functions scaled using fitted barrier heights and positions from Table IV, as discussed in the text.

To summarize, up to this point we have found that there is a complex, not unsystematic, response of the fusion excitation functions, at sub-barrier energies, to changes in nuclear structure of target and projectile. Substantially more sub-barrier fusion is observed than can be accounted for by adiabatic penetration by spherical, liquid-drop nuclei. Increases in fusion arising from zero-point motion are insufficient to explain the large differences.

IV. PHENOMENOLOGICAL ANALYSIS

In order to provide further insight into the significance of the data we performed a phenomenological barrier penetration analysis. This analysis was guided by several observations. First, there were the clear indications in Figs. 6 to 8 of a dynamic

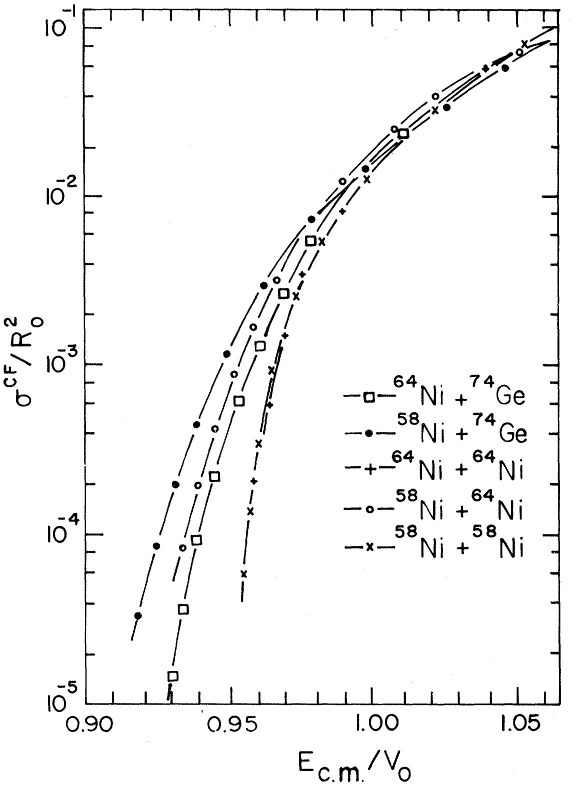

FIG. 8. Reduced excitation functions, as in Fig. 7, using radial positions from Table V.

influence of valence neutrons, and of softness. Second, there were difficulties encountered in an initial analysis of the data. These problems will be discussed in detail shortly. Finally, there were results of several pertinent Hartree-Fock calculations.

The starting point for the phenomenological analysis was the decomposition of the complete fusion cross sections into contributions from each partial wave

$$\sigma^{CF} = \pi \lambda\!\!\!^{-2} \sum_l (2l+1) T_l , \tag{1}$$

where $\lambda\!\!\!^{-}$ is the reduced de Broglie wavelength of the incident ion. The quantity T_l denotes the transmission coefficient, for the lth partial wave, for passage either through or over the interaction barrier maximum. Implicit in Eq. (1) are the Kaufman-Wolfgang condition[1] and the assumption of IWBC.[2,3] To determine the transmission coefficients we employed the WKB method relationship[6]

$$T_l = (1 + \exp 2K_l)^{-1} \tag{2a}$$

with

$$K_l = \mp \int_{r_a}^{r_b} \left[\frac{2M(r)}{\hbar^2} \mid V_l(r) - E \mid \right]^{1/2} dr . \tag{2b}$$

Equation (2) is valid for barriers which obey appropriate mathematical conditions.[6] Those conditions are satisfied for the approximate parabolic barriers of interest in this work. The constants r_a and r_b denote the classical turning points of the interaction barrier $V_l(r)$ at the center-of-mass energy E, and the $-$ and $+$ signs refer to above and below barrier energies, respectively.

We then introduced an interaction potential of the form

$$V_l(r) = V_{\text{Coul}}(r) + V_{\text{cent}}(r) + V_{\text{nuc}}(r) , \tag{3}$$

where

$$V_{\text{Coul}}(r) = \begin{cases} \left[\dfrac{\alpha}{R_{\text{Coul}}} - \dfrac{\beta r^2}{R_{\text{Coul}}{}^3} \right] Z_T Z_P e^2 & r < R_{\text{Coul}} \\[2ex] \dfrac{Z_T Z_P e^2}{r} , & r \geq R_{\text{Coul}} \end{cases} , \tag{4}$$

$$V_{\text{cent}}(r) = \frac{\hbar^2 l(l+1)}{2M(r) r^2} , \tag{5}$$

and

$$V_{\text{nuc}}(r) = -V_{\text{WS}} \left[1 + \exp \frac{r - R_{\text{WS}}}{a_{\text{WS}}} \right]^{-1} . \tag{6}$$

For the Coulomb potential we used an approximate expression for uniform charge distributions. The constants α and β were determined by requiring continuity of the potential and its first derivative at the matching radius R_{Coul}. We took the nuclear potential to be of a Woods-Saxon form. Exponential and Yukawa forms were also used; the particular choice of exponential-like potential had little effect upon the results of interest.

The fusion process is characterized by shape degrees of freedon as well as by radial separation. The occurrence of softness in the shape degrees of freedom gives rise to alternate fusion paths. These alternate paths are not taken into account in standard one-dimensional approaches. The quantity $M(r)$ appearing in the expression for the action integral and in the expression for the centrifugal potential is an effective mass. For well-separated nuclei, it equals the reduced mass; for interacting nuclei, it can reach values considerably less than the reduced mass. We propose to use this quantity to

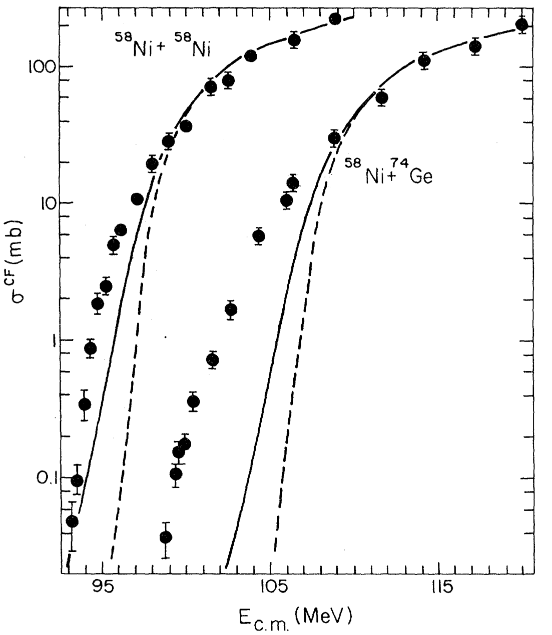

FIG. 9. Comparisons of experimental and phenomenological excitation functions for complete fusion. Filled circles represent the experimental results. Dashed curves denote results of calculations performed using $V_{\rm int}$ from Eq. (7). Solid curves represent results of calculations performed using Eq. (3). The value for $R_{\rm Coul}$ used in all calculations was 1.18 fm $(A_T^{1/3}+A_P^{1/3})$. The Woods-Saxon constants and corresponding mean effective masses are listed in Table V. The evaluation of Eqs. (1)–(8) was done by means of numerical integration using a code specifically written (Ref. 15) for that purpose.

take into account alternate fusion paths. Evidence for softness has been provided by the Hartree-Fock calculations of Negele and Rinker.[13] In these calculations the authors demonstrate that nuclei in the nickel-zinc region have nearly flat energy-of-deformation versus mass quadrupole moment curves, i.e., these nuclei are exceedingly soft with respect to shape deformations. Evidence that an effective mass can be used to take into account shape degrees of freedom has been provided by the Hartree-Fock calculations of Flocard, Heenen, and Vautherin.[14]

Initially, we considered an interaction potential of the form

$$V_l(r)=\begin{cases} V_{\rm Coul}(r)+\dfrac{\hbar^2 l(l+1)}{2\mu r^2}+V_{\rm nuc}(r) & r>R_x \\ V_0-\frac{1}{2}\mu\omega_0^2(r-R_0)^2+\dfrac{\hbar^2 l(l+1)}{2\mu r^2} & r\le R_x \end{cases} \tag{7}$$

with matching radius $R_x>R_0$. In Eq. (7) an inverted harmonic oscillator potential was joined to a Coulomb plus nuclear plus centrifugal tail. The nuclear potential was fixed by the requirement that the magnitude and slope of the interaction potential was continuous at R_x. The reduced mass μ was used in $V_{\rm cent}(r)$ and in K_l. The quantities V_0, R_0, and $\hbar\omega_0$ denote the height, position, and curvature of the s-wave interaction barrier maximum. In the analysis, $\hbar\omega_0$ was fixed at 4 MeV and the fusion barrier heights and positions were deduced by fitting to the above-barrier portion of the excitation functions.

The excitation functions calculated in this manner for the systems exhibiting the least and most sub-barrier fusion, namely ^{58}Ni + ^{58}Ni and ^{58}Ni + ^{74}Ge, are displayed in Fig. 9. The energy ranges spanned by the fitted, above-barrier portions of the excitation functions are listed in column 6 of Table IV. The heights and positions of the interaction barrier maximum deduced from these fits are presented in columns 2 to 4. These quantities were used in constructing the reduced excitation functions displayed in Fig. 7. The calculated excitation functions had slopes, at above-barrier energies, which were in better agreement with the data than the corresponding liquid-drop calculations presented in Refs. 4 and 5. The calculated excitation functions also had magnitudes, at far sub-bar-

TABLE IV. Summary of interaction barrier maxima deduced using Eq. (7).

System	V_0 (MeV)	R_0 (fm)	r_0 (fm)	$\hbar\omega_0$ (MeV)	$E_{\rm c.m.}/V_0$
^{58}Ni + ^{58}Ni	97.9	8.30	1.07	4.0	1.01–1.11
^{58}Ni + ^{64}Ni	96.0	8.20	1.04	4.0	1.01–1.14
^{64}Ni + ^{64}Ni	93.5	8.60	1.08	4.0	1.01–1.14
^{58}Ni + ^{74}Ge	107.5	8.00	0.99	4.0	1.01–1.12
^{64}Ni + ^{74}Ge	105.1	8.20	1.00	4.0	1.02–1.09

rier energies, which were closer to those of the data than the above-mentioned liquid-drop results.

The most significant feature of the analysis was the radial positions listed in Table IV. From the values for $r_0 = R_0/(A_T^{1/3} + A_P^{1/3})$ given in column 4, we saw that the barrier maxima occurred near or beyond saturation density. We investigated this aspect further by examining the nuclear potentials which generated such maxima. We found form factors which could not, in principle, describe elastic scattering. For example, to produce a barrier height of 97.9 MeV at 8.46 fm for the ^{58}Ni + ^{58}Ni system, we needed an $r_{\rm WS} = 0.76$ fm and an $a_{\rm WS} = 2.12$ fm for $V_{\rm WS} = 150$ MeV. In addition, we found that there were difficulties, even for moderate l values, with the Kaufman-Wolfgang[1] condition.

We now return to our model given by Eqs. (1)–(6). The effective mass in our model was chosen to have the simple form

$$M(r) = \mu\left[1 - \kappa f(r)\right], \tag{8a}$$

where $f(r)$ is a Fermi function

$$f(r) = \left[1 + \exp\frac{r - R_M}{a_M}\right]^{-1} \tag{8b}$$

whose use ensures the proper asymptotic behavior. The geometric constants $r_M = R_m/(A_T^{1/3} + A_P^{1/3})$ and a_M were fixed by the criteria that (i) the departures of the effective mass from the reduced mass diminish to 10% of the total at the outer turning-point of $V_0(r)$, at the lowest relevant energy; (ii) the lowering of the effective mass reach 90% of the full change by the inner turning point of $V_l(r)$, for the highest relevant l value and energy. To satisfy this criteria, knowledge of $V_{\rm cent}(r)$ was needed which, in turn, involved specification of $M(r)$. The simple iterative procedure used in the code required only a few steps for convergence. The criteria yielded an effective mass with a mean value $M = \mu[1 - \kappa/2]$ well centered on the $V_l(r)$, and having an acceptable radial dependence. A representative $V_l(r)$ and corresponding $M(r)$ as shown in Fig. 10.

We then selected a Woods-Saxon well depth and a form factor of the elastic scattering type; in particular, we took $V_{\rm WS} = 100$ MeV, $r_{\rm WS} = 1.20$ fm, and $a_{\rm WS} = 0.60$ fm. We performed those minor adjustments needed to reproduce the barrier heights already given in Table IV. The final step was to vary only κ, seeking a value which, when used in Eqs. (2), (3), and (8), would enable us to reproduce the same above-barrier portion of the excitation functions as done in the initial analysis.

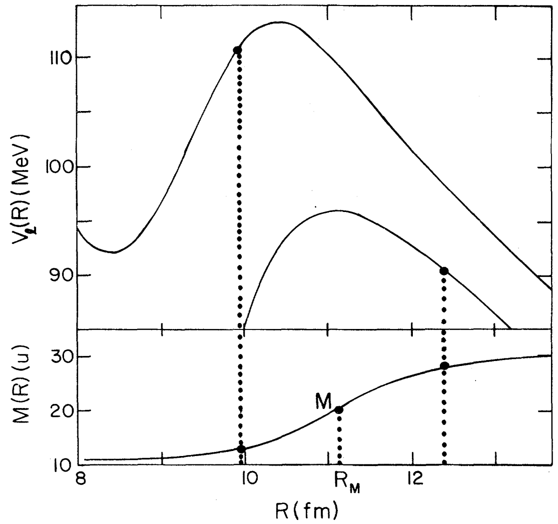

FIG. 10. Plot of (a) the barrier portion of the interaction potential from Eq. (3), for $l = 0$ and $40\hbar$, and (b) the effective mass from Eq. (8), vs radial separation for the ^{58}Ni + ^{64}Ni system. Woods-Saxon constants and mean effective mass, M, are given in Table V. The dotted guide lines indicate the locations of the turning points used to generate the Fermi function constants $r_M = 1.42$ fm, and $a_M = 0.56$ fm.

The resulting Woods-Saxon constants and mean effective masses are presented in Table V. The radial positions listed in column 6 and the barrier heights listed in Table IV were used in constructing the reduced excitation functions presented in Fig. 8. The calculated excitation functions are shown in Figs. 9 and 11. As can be seen, the above-barrier portions of the experimental excitation functions are well reproduced. We have a nuclear potential which can, in principle, describe elastic scattering, and the interaction barrier maxima are properly located in the surface region. Variations among the constants appearing in Table V are minor; we have, in effect, described the above-barrier portion of the five excitation functions with a single standard Woods-Saxon potential plus effective mass.

At sub-barrier energies, the calculated excitation functions are orders of magnitude closer to the data than previously obtained. For ^{58}Ni + ^{58}Ni and ^{64}Ni + ^{64}Ni the calculated cross sections approach the experimental values. For the other systems the model predicts a factor of 30 to a factor of 70 too little fusion. No attempt has been made to improve the sub-barrier results for any system by

TABLE V. Woods-Saxon potentials, positions of interaction barrier maxima, and corresponding mean effective masses deduced using Eq. (3).

System	V_{WS} (MeV)	R_{WS} (fm)	r_{WS} (fm)	a_{WS} (fm)	R_0 (fm)	r_0 (fm)	M (u)
^{58}Ni + ^{58}Ni	100	9.21	1.190	0.60	10.9	1.40	19.1
^{58}Ni + ^{64}Ni	100	9.41	1.196	0.60	11.1	1.41	20.7
^{64}Ni + ^{64}Ni	100	9.70	1.212	0.60	11.4	1.43	20.8
^{58}Ni + ^{74}Ge	100	9.72	1.204	0.60	11.3	1.40	20.8
^{64}Ni + ^{74}Ge	100	9.97	1.216	0.60	11.6	1.42	22.0

parameter adjustments. It is noteworthy that the Hartree-Fock approach treats within a common framework many of the single-particle and global effects discussed in Refs. 4 and 5. Our phenomenological representation of the rich, microscopic approach by a single radially-dependent effective mass and a standard Woods-Saxon potential is a simplification. Furthermore, the effective mass may depend in some complicated manner upon impact parameter (angular momentum) and bombarding energy. The neglect of such a dependence is least important at sub-barrier energies and most important at above-barrier energies. Lastly, we note that the effective mass appearing in the expression for the action integral is not necessarily indentical to the effective mass appearing in the expression for the centrifugal potential.

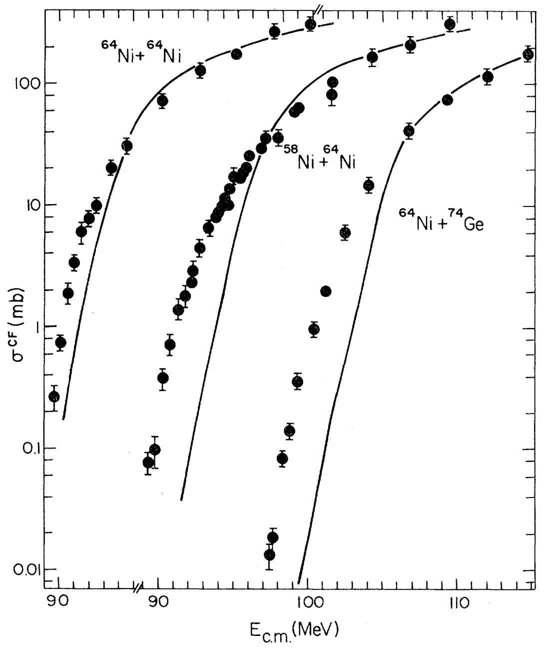

FIG. 11. Comparisons of experimental and phenomenological excitation functions for complete fusion. Filled circles represent the experimental results. Solid curves denote results of calculations performed using Eq. (3), as in Fig. 9.

Our final observation is that the slopes of the calculated excitation functions do not vary as rapidly as the slopes of the experimental excitation functions, at far sub-barrier energies. This shortcoming can be overcome[16] either by introducing a thickening of the interaction barriers just inside the maxima or by introducing a depression in the maxima. In the latter instance, situations can occur in which the lowest energy regime is dominated by the outer barrier and the higher energy portion by the inner barrier. Lacking theoretical justification, such potentials remain, at present, only an interesting possibility.

The variations in agreement between data and calculations shown in Figs. 9 and 11 parallel the variations exhibited by the reduced excitation functions. These variations in agreement may be due to dynamic, single-particle processes such as the transfer or exchange of nucleons, particularly pairs. These processes might occur near or at the distance of closest approach and serve as an initial stage of the fusion reaction. Increases in sub-barrier fusion would take place in those systems whose nuclear structure favors such bonding processes. Corresponding variations in sub-barrier transfer cross sections should exist, as well.

The sub-barrier fusion reaction involves multidimensional barrier penetration, nuclear structure, and nuclear dynamics. One open question is the behavior of the nuclear and ion-ion potentials near the inner turning point of the interaction barrier where the density overlap may be appreciable. There are open questions with respect to dynamic polarization and deformations, as well. The central importance of the Hartree-Fock approach has already been pointed out in this work. Some recent alternative approaches and viewpoints are presented in Ref. 17.

V. SUMMARY

Differential cross sections for evaporation residue formation following complete fusion of ^{64}Ni and ^{74}Ge with 171 to 215 MeV ^{58}Ni and ^{64}Ni ions were measured with high precision using the MIT-BNL recoil mass selector together with a counter telescope. Angular distributions were measured in $\frac{1}{2}$° or 1° steps from 0° to 6°. Recoil kinetic energy spectra and supplemental zero-degree differential cross sections were measured. The resulting excitation functions for complete fusion ranged in magnitude from 10 μb to 300 mb.

In order to compare the Ni-Ni results with the Ni-Ge results we constructed reduced excitation functions. Significant variations remained after removal of the barrier height and position dependence. The ^{58}Ni + ^{74}Ge system exhibited the most sub-barrier fusion; the ^{58}Ni + ^{58}Ni and ^{64}Ni + ^{64}Ni systems exhibited the least sub-barrier fusion. The Ni-Ni isotopic variations, the Ni vs Ge differences, and the overall large amount of sub-barrier fusion relative to liquid-drop predictions all provide evidence that the observed fusion resulted from dynamic, single-particle/softness-related processes.

A straightforward phenomenological analysis was performed; in this analysis a radially-dependent effective mass was employed. The use of the effective mass led to a meaningful description of our above-barrier data and to improvements towards reproducing our sub-barrier data.

ACKNOWLEDGMENTS

The authors wish to acknowledge valuable discussions with H. A. Enge, A. K. Kerman, J. W. Negele, and J. R. Nix. This work was supported by the U. S. Department of Energy under Contract No. DE-AC02-76ER03069.

---

[*] Deceased.

[†] Present address: Physics Department, Stanford University, Stanford, California 94305.

[‡] Present address: Physics Department, United States Military Academy, West Point, New York 10996.

[1] R. Kaufman and R. Wolfgang, Phys. Rev. 121, 192 (1961).

[2] H. Feshbach, D. C. Peaslee, and V. F. Weisskopf, Phys. Rev. 71, 145 (1947).

[3] H. A. Bethe, Phys. Rev. 57, 1125 (1940).

[4] M. Beckerman, M. Salomaa, A. Sperduto, H. Enge, J. Ball, A. DiRienzo, S. Gazes, Yan Chen, J. D. Molitoris, and Mao Nai-feng, Phys. Rev. Lett. 45, 1472 (1980).

[5] M. Beckerman, J. Ball, H. Enge, A. Sperduto, S. Gazes, A. DiRienzo, and J. D. Molitoris, Phys. Rev. C 23, 1581 (1981).

[6] E. C. Kemble, Phys. Rev. 48, 549 (1935).

[7] J. M. Alexander and L. Winsberg, Phys. Rev. 121, 529 (1961).

[8] J. J. Krappe, J. R. Nix, and A. J. Sierk, Phys. Rev. Lett. 42, 215 (1979); Phys. Rev. C 20, 992 (1979).

[9] J. Błocki, J. Randrup, W. J. Swiatecki, and C. F. Tsang, Ann. Phys. (N.Y.) 105, 427 (1977).

[10] S. Landowne and J. R. Nix, Nucl. Phys. A368, 352 (1981).

[11] P. Möller and J. R. Nix, Nucl. Phys. A361, 117 (1981).

[12] C. Y. Wong, Nucl. Data A4, 271 (1968).

[13] J. W. Negele and G. Rinker, Phys. Rev. C 15, 1499 (1977).

[14] H. Flocard, P. H. Heenen, and D. Vautherin, Nucl. Phys. A339, 336 (1980).

[15] M. Beckerman (unpublished).

[16] M. Beckerman, M. Salomaa, and A. DiRienzo, Bull. Am. Phys. Soc. 26, 555 (1981).

[17] H. Esbensen, Nucl. Phys. A352, 147 (1981); R. G. Stokstad and E. E. Gross, Phys. Rev. C 23, 281 (1981); L. C. Vaz, J. M. Alexander, and G. R. Satchler, Phys. Rep. 69C, 373 (1981).